Research Square

Preprints are preliminary reports that have not undergone peer review.
They should not be considered conclusive, used to inform clinical practice,
or referenced by the media as validated information.

Particle-Enhanced Temperature-Sensitive Paint: Development and Validation for High-Speed Aerothermodynamic Testing

Jinyoung Kim
Seoul National University
Mithat Engin
Technical University of Berlin
Masaki Okawa
Tohoku University
Tsubasa Ikami
Tohoku University
Bok Jik Lee
Seoul National University
Hiroki Nagai
nagai.hiroki@tohoku.ac.jp

Tohoku University

Research Article

Keywords: Temperature-Sensitive Paint, Heat Flux Measurement, Hypersonic Flow

Posted Date: March 3rd, 2026

DOI: https://doi.org/10.21203/rs.3.rs-8884315/v1

License: This work is licensed under a Creative Commons Attribution 4.0 International License.
Read Full License

Additional Declarations: No competing interests reported.

Version of Record: A version of this preprint was published at Experiments in Fluids on July 31st, 2026.
See the published version at https://doi.org/10.1007/s00348-026-04282-3.

Particle-Enhanced Temperature-Sensitive Paint: Development and Validation for High-Speed Aerothermodynamic Testing

Jinyoung Kim[1], Mithat Engin[2], Masaki Okawa[3,4], Tsubasa Ikami[4], Bok Jik Lee[5], Hiroki Nagai[4*]

[1]Department of Aerospace Engineering, Seoul National University, Seoul 08826, Republic of Korea.
[2]Institute of Aeronautics and Astronautics, Technical University of Berlin, Berlin 10587, Germany.
[3]Department of Aerospace Engineering, Tohoku University, Sendai, Miyagi 980–8579, Japan.
[4*]Institute of Fluid Science, Tohoku University, Sendai, Miyagi 980–8577, Japan.
[5]Institute of Advanced Aerospace Technology, Seoul National University, Seoul 08826, Republic of Korea.

*Corresponding author(s). E-mail(s): nagai.hiroki@tohoku.ac.jp;
Contributing authors: kimted@snu.ac.kr; mithat.engin@outlook.de; okawa.masaki.t3@dc.tohoku.ac.jp; tsubasa.ikami.c5@tohoku.ac.jp; b.lee@snu.ac.kr;

Abstract

Accurate measurement of surface temperature of high-speed vehicles, such as atmospheric entry capsules and space exploration vehicles, is critical for the design of thermal-protection systems and the development of thermal-load mitigation strategies. Temperature-sensitive paint (TSP) has emerged as a pivotal non-intrusive method for global heat flux measurement in ground-testing facilities. However, conventional TSP formulations suffer under extreme flow

conditions, including self-illumination by nozzle flow, rapid fluctuations in temperature and pressure, and low signal-to-noise ratios. To address these challenges, this study presents a particle-enhanced TSP (PE-TSP) incorporating calcium silicate microparticles to increase luminescence intensity, improve temperature sensitivity, and minimize pressure dependency. Development and characterization tests revealed performance gains over a standard TSP formulation: luminescence intensity increased by 21%, temperature sensitivity increased by 11%, and pressure dependency was reduced by twice. For validation, both PE-TSP and the standard TSP were applied in a shock tube test section to assess dynamic response to extreme flow condition. The result showed that, owing to the increased signal-to-noise ratio, PE-TSP reduced the standard deviation by up to 33%. These results confirm the applicability of PE-TSP for high-speed aerothermodynamic diagnostics.

Keywords: Temperature-Sensitive Paint, Heat Flux Measurement, Hypersonic Flow

1 Introduction

The management of surface temperature using thermal protection systems and thermal load reduction technologies is a critical consideration in the design of high-speed vehicles, including atmospheric entry capsules and space exploration vehicles. Especially under high-Mach and high-enthalpy conditions, phenomena such as chemical and thermal non-equilibrium, boundary layer transition, and unsteady shock wave/boundary layer interactions arise, presenting significant challenges for both experimental measurement and numerical modeling. Ground-based high-speed aerothermodynamic facilities, such as the SNU Hypersonic Shock Tunnel (SHyST) at Seoul National University (Kim et al. 2025), the High Enthalpy Shock Tunnel (HIEST) at JAXA (Tanno et al. 2009), and the T4 Shock Tunnel at the University of Queensland (Paull and Stalker 1998), have been developed to investigate these phenomena. Heat flux measurements in such experiments typically rely on intrusive sensors such as thermocouples and thin-film gauges. However, improper sensor alignment on the model surface can disturb boundary layer generation, leading to inaccurate measurements. Additionally,

these sensors provide only localized, point-wise data, limiting their effectiveness in capturing global heat flux distributions. Furthermore, the millisecond-scale test durations characteristic of impulse ground-testing facilities such as those mentioned above further demand sensors with both high sensitivity and fast response, often at significant cost.

Temperature-sensitive paint (TSP) offers a non-intrusive alternative for global surface heat flux measurement through temperature-dependent luminecent emission. When excited by the absorption light, luminescent dye in the paint emits flourescence at a longer wavelength. The emission intensity I, and the local temperature T exhibit an inverse relationship governed by Arrhenius equation (Liu et al. 2021):

$$\frac{I(T)}{I(T_{ref})} = exp\left(\frac{E}{R}\left(\frac{1}{T} - \frac{1}{T_{ref}}\right)\right) \tag{1}$$

where I_{ref} and T_{ref} denote the intensity and temperature at a reference state, E is the activation energy for non-radiative process, and R is the universal gas constant. Utilizing this mechanism, TSP has been applied across a wide range of aerothermodynamic studies, from subsonic to hypersonic flows, and from cryogenic to high-temperature environment. Lang et al. (2015) used TSP to detect boundary layer transition on rotor blades, while Ikami et al. (2015) combined a carbon-nanotube layer with TSP to achieve simultaneous surface heating and temperature mapping on rotating blades, capturing leading edge vortex developement with increasing angle of attack. Petersen and Hilfer (2024) used TSP to examine the effect of surface roughness on boundary layer transition in high-pressure turbine vanes. Fey et al. (2003) employed TSP in a cryogenic transonic wind tunnel to identify transition on wing assemblies. Ozawa (2016) and Ozawa and Laurence (2018) characterized unsteady aerothermodynamic phenomena and shock-induced flow over a wall mounted cylinder in a shock tube test section.

TSP has been also applied in hypersonic ground-testing facilities (Nakakita et al. 2003; Nagai et al. 2011; Ozawa et al. 2015; Nagayama et al. 2016; Martinez Schramm et al. 2017; Laurence et al. 2019; Risius et al. 2017), yet its implementation in these environments presents several challenges. Test durations are limited to a few milliseconds, requiring fast response, high temperature sensitivity, and high luminescent intensity to capture transient data with adequate temporal resolution. Also, TSP's luminescent dye can be quenched by oxygen, resulting in unwanted pressure-dependent output. Moreover, self-luminescence from high-enthalpy test gases degrades the signal-to-noise ratio (SNR) and introduces error into surface heat flux measurements (Nagayama et al. 2017; Martinez Schramm et al. 2017).

Several strategies have been proposed to mitigate these limitations. Horagiri and Nagai (2014) incorporated calcium silicate ($CaSiO_3$) microparticles into a TSP based on dichlorotris(1,10-phenanthroline)ruthenium(II) hydrate (Ru(phen)), reporting enhanced luminescence intensity; however, neither detailed characterization of the particle-augmented formulation nor optimization of Ru(phen) concentration was performed. At the same laboratory, Ikami et al. (2022) subsequently optimized the concentrations of Ru(phen) and the polyacrylic acid (PAA) binder to maximize temperature sensitivity, but did not evaluate the combined effect of particle addition. Beyond these studies, several research groups have developed TSPs using various dye and polymer binder combinations to improve performance (Egami et al. 2012; Peng et al. 2016; Martinez Schramm et al. 2017); however, systematic evaluation of luminescence enhancement and particle-induced effects has not been reported.

Building on this legacy, the present study develops a particle-enhanced TSP (PE-TSP) by integrating optimized Ru(phen)/PAA formulations with $CaSiO_3$ microparticles to enhance the SNR under extreme flow conditions at impulse ground-testing facilities. Comprehensive characterization of PE-TSP is conducted to assess luminescence intensity, temperature sensitivity, pressure dependency, and photodegradation.

Finally, performance improvements are validated in the square shock tube test section at Tohoku University.

2 PE-TSP Formulation and Experimental Methods

The objective of the present TSP development is to increase the SNR within the short test durations characteristic of impulse facilities. The target operational temperature range is 10–70 °C, corresponding to test conditions in which the total enthalpy is below $h_{\mathrm{total}} \approx 3$ MJ/kg. To meet this objective, the TSP must exhibit: (1) fast response time, (2) high temperature sensitivity, (3) high luminescent intensity, and (4) low pressure sensitivity. These characteristics are determined by both material selection and optimization of concentration ratios.

2.1 Material Selection

Conventional TSP formulations consist of a luminescent dye, a polymer binder, and a solvent. In this work, Ru(phen) was selected as the luminophore due to its microsecond (< 1 μs) luminescence lifetime (Hubner et al. 2001, 2002) and high temperature sensitivity near room temperature. It exhibits an absorption peak at approximately 450 nm and an emission peak at approximately 580 nm. PAA was chosen as the binder, as previous studies have demonstrated its ability to suppress pressure dependency when combined with Ru(phen) (Ikami et al. 2022). PAA's glass transition temperature is $T_g \approx 106$ °C (Liu et al. 2021), which is sufficient for the intended operating range.

$CaSiO_3$ microparticles were incorporated into the Ru(phen)/PAA formulation to develop the PE-TSP. The addition of silicate-based particles was motivated by their previously reported benefits in improving luminescence performance for high-efficiency LED applications (Woo et al. 2023), as well as their ability to reduce oxygen-quenching effects and enhance photostability (Othman et al. 2021; Liu et al. 2017). Among several particle candidates evaluated in previous studies, $CaSiO_3$ demonstrated the highest

relative increase in luminescence intensity (Horagiri and Nagai 2014). A particle size range of 7–10 μm was selected as the smallest commercially available option, offering a practical balance between optical performance and cost. The material selection criteria and corresponding choices are summarized in Table 1.

Table 1: A summary of TSP material selection criteria and formulation

Material	Selection criteria	Chosen material (manufacturer)	Abbreviation
Luminescent dye	(1) fast response time (2) high temperature sensitivity	dichlorotris (1,10-phenanthroline) ruthenium (II) hydrate (Merck KGaA)	Ru(phen)
Polymer binder	(4) low pressure dependency	polyacrylic acid (FUJIFILM Wako Chemicals)	PAA
Microparticle	(2) high temperature sensitivity (3) strong luminescent intensity (4) low pressure dependency	calcium silicate (Merck KGaA)	$CaSiO_3$
Solvent	-	ethanol (FUJIFILM Wako Chemicals)	EtOH

2.2 Specimen Preparation

All TSP specimens were prepared following the same procedure. A white basecoat (MH12006, Musashi Holts) was uniformly applied to the aluminum substrate to provide optical and thermal isolation and to serve as a reflective underlayer. The basecoat was dried for 24 hours under vacuum at 10 kPa (absolute). The TSP layer was then spray-applied onto the basecoat and dried under the same vacuum conditions. Because $CaSiO_3$ is insoluble in the PAA–ethanol system and exhibits limited suspension stability, the TSP mixture was continuously agitated with an ultrasonic mixer during spraying to maintain uniform particle dispersion and to suppress local particle agglomeration that could otherwise introduce spatial thermal property inhomogeneity within the coating. Each layer's thickness was controlled by the number of spray

strokes to ensure reproducibility across specimens. Thickness measurements were performed using a scanning electron microscope (SEM, VE-9800, Keyence). On average, the basecoat thickness was 18.5 ± 0.5 μm, while the TSP layer thickness (L_p) was 2.2 ± 0.6 μm. The L_p was intentionally kept much smaller than that of the basecoat to ensure fast temporal response, as the thermal response time τ scales with the square of the layer thickness according to $\tau \propto L_p^2/\alpha_p$, where α_p is the thermal diffusivity of the TSP.

2.3 Concentration Optimization

To maximize the emission intensity and temperature sensitivity of the Ru(phen)/PAA-based TSP, both the dye concentration (C_{dye}) and particle concentration (C_{particle}) require careful optimization. The dye concentration is defined as

$$C_{\mathrm{dye}}\ (\mathrm{mg/g}) = \frac{m_{\mathrm{dye}}\ (\mathrm{mg})}{m_{\mathrm{polymer}}\ (\mathrm{g})} \tag{2}$$

where m_{dye} and m_{polymer} are the masses of dye and polymer, respectively. Ikami et al. (2022) previously identified $C_{\mathrm{dye}} = 100$ mg/g as the optimum for Ru(phen)/PAA, yielding maximum temperature sensitivity. Accordingly, this value was adopted in the present study as the baseline for further optimization. For performance comparison, a concentration of 50 mg/g, referred to as the reference case ($\mathrm{TSP_{ref}}$), was also examined, as suggested by Liu et al. (2021) and used in prior studies by the same laboratory (Horagiri and Nagai 2014; Nagayama et al. 2016, 2017).

The optimization parameter in this study is the particle concentration C_{particle}, defined as the weight percentage of $CaSiO_3$ relative to the total solid content in the Ru(phen)/PAA solution. $CaSiO_3$ was incorporated at concentrations ranging from 0 to 50 wt.%, and the emission intensity and temperature sensitivity were compared

across cases. A total of nine formulations were prepared, including the reference case without particle addition, as summarized in Table 2.

Table 2: Optimization cases for $CaSiO_3$ concentration.

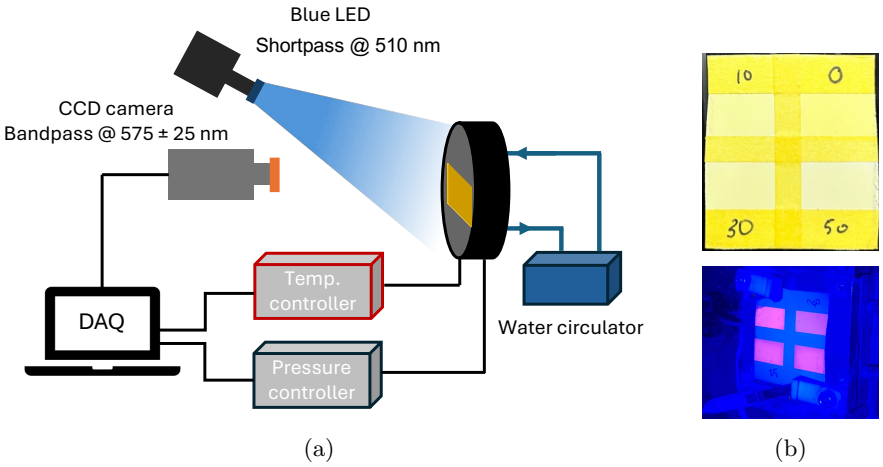
C_{dye} [mg/g]	50 (TSP_{ref})	100	100	100	100	100	100	100	100
$C_{particle}$ [wt.%]	0	0	5	10	15	20	25	30	50
Test plate No.	1,2,3	2	2	1	2	3	3	1	1

2.4 Experimental Setup for Optimization and Characterization

To evaluate the effects of particle concentration, both optimization and characterization were conducted under controlled conditions. For the optimization study, emission intensity and temperature sensitivity were evaluated. For the characterization, in addition to these two parameters, pressure dependency and photodegradation were investigated, complemented by detailed surface morphology analysis using SEM imaging.

A pressure- and temperature-controlled calibration chamber was employed for these measurements, as illustrated in Fig. 1a. The chamber accommodates a surface temperature range of 5–65 °C, regulated using a Peltier plate (PU-50WS, Takagi MFG) coupled with a temperature controller (TDU-5000ARG, Cell System) and a water circulator. Chamber pressure is adjustable from 10 Pa to 200 kPa using a precision pressure controller (PACE6000, Baker Hughes). A blue LED light source with a peak wavelength of 462 nm (IL-106B, HARDsoft) was used to excite the Ru(phen) dye molecules in the TSP. The emitted luminescence was recorded using a 16-bit CCD camera (C4742-98 KAG2, Hamamatsu Photonics) paired with 50 mm lens (AF-S NIKKOR 50mm F1.4G, Nikon). A 510 nm shortpass filter (SV0510, Asahi Spectra) and a heat-absorbing filter (HAF-50 S-30 H, Sigma Koki) were placed in front of the

LED light source to suppress unwanted longer-wavelength components, while a 575 ± 25 nm bandpass filter was mounted in front of the camera to selectively capture the emission peak and suppress scattered excitation light, as shown in Fig. 2.



(a) (b)

Fig. 1: (a) Schematic of a calibration chamber, (b) image of test plate (No.3) before (top) and during (bottom) illumination.

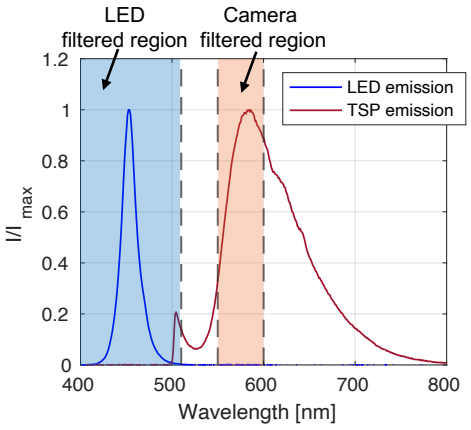


Fig. 2: Emission spectra of the LED light source and Ru(phen)-based TSP, with the optically filtered detection band used in the experiments. Note that the TSP emission spectrum was measured with a 500 nm high-pass optical filter.

Emission intensity $I(T)$, was measured over a temperature range from 14 °C to 64 °C, in increments of 2 °C. To minimize errors caused by illumination and imaging nonuniformity during each calibration test, four optimization cases were coated on a single aluminum test plate (40 mm × 45 mm × 1 mm) and placed together in the calibration chamber, as shown in Fig. 1b. In total, three such plates were prepared, as summarized in Table 2, each including $\mathrm{TSP_{ref}}$ for normalization ($\mathrm{I/I_{TSP_{ref}}}$) in relative intensity comparisons. The temperature sensitivity, S_T, was calculated as

$$S_T\ (\%/^\circ\mathrm{C}) = -\frac{dI(T)}{dT} \cdot \frac{1}{I(T)} \times 100 \tag{3}$$

The resulting sensitivity data were fitted with a seventh-order polynomial for subsequent analysis. Photodegradation tests were performed at 20 °C and 100 kPa over 130 minutes of continuous illumination. Pressure dependency was characterized inside a shock tube facility to achieve a wider pressure range than the calibration chamber, with pressures varied from 100 kPa to 500 kPa at 20 °C.

2.5 Experimental Setup for Shock Tube Validation

To validate the performance improvement in SNR, comparative tests of PE-TSP and $\mathrm{TSP_{ref}}$ were conducted using the square shock tube at Tohoku University, as shown in Fig. 3. The shock tube provides a well-controlled environment with sharp, repeatable transients leading to high temperatures and pressures within millisecond-scale test time. These characteristics make it well suited for preliminary validation prior to application in more extreme environments, such as high-enthalpy and hypersonic flows.

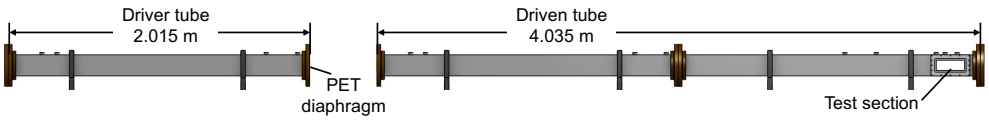


Fig. 3: Schematic of TU square shock tube.

TSPs were applied to two regions of the test section, as illustrated in Fig. 4: the end wall and the side wall. The end wall is located at the triple point, where a single strong shock passes through, resulting in a stagnation condition. Because only a small region was observed, the camera was operated at a high frame rate of 840,000 fps (approximately 1 μs per frame). Combined with the relatively long test duration after the triple point ($\sim$ 2 ms), this configuration is well suited for obtaining thermophysical properties through *in-situ* calibration, as discussed later in this section. In contrast, the side wall was used to capture dynamic and unsteady flow phenomena. Since the observed region was larger than that of the end wall, the camera frame rate was reduced to 200,000 fps, resulting in 5 μs per frame. This configuration allows observation of incident and reflected shocks, which develop on the order of 0.1 ms, as well as subsequent turbulent boundary-layer growth and streak formation.

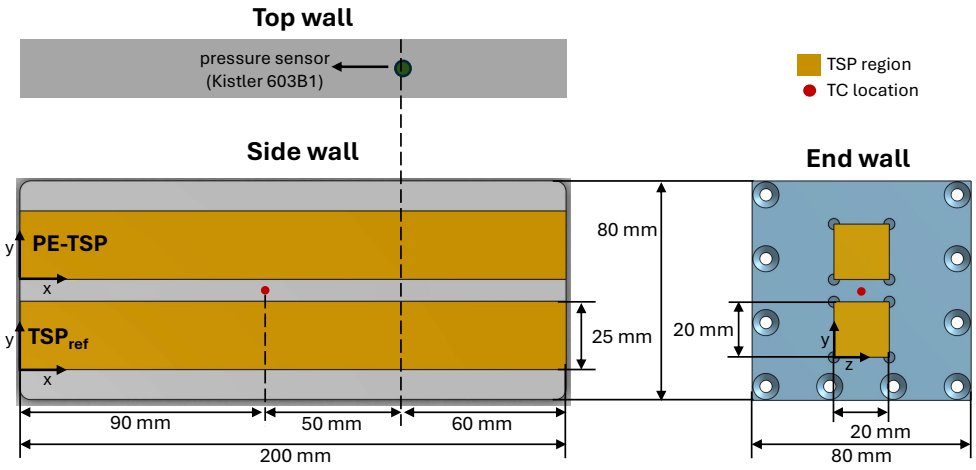


Fig. 4: Shock tube test section configuration.

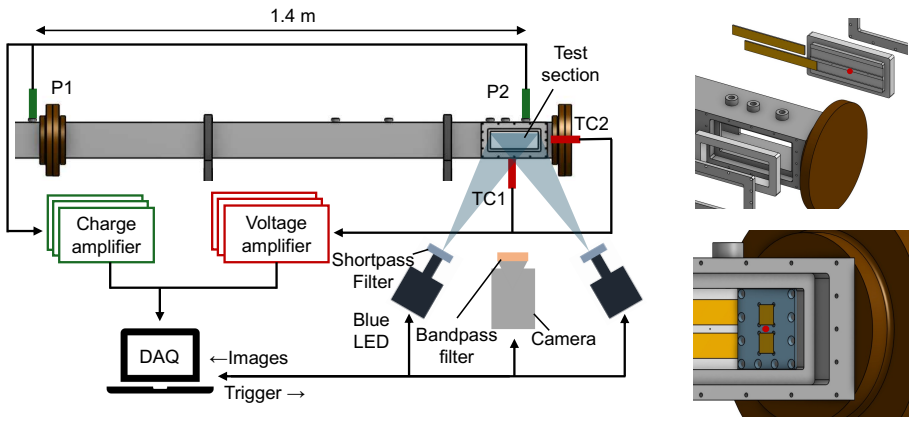
For quantitative comparison of SNR improvement, three measurement locations were analyzed: (1) end wall at $x = 200$ mm, (2) side wall–downstream at $x = 195$ mm, and (3) side wall–upstream at $x = 90$ mm. The side wall–upstream position coincides with TC1, while the end wall and side wall–downstream positions correspond

to TC2. For the end wall and side wall–downstream cases, the mean and standard deviation (STD) of the heat flux were computed over a 0.9 ms window after the triple point. This interval was used both to evaluate SNR improvement and to validate the thermophysical parameter $\sqrt{\rho_b c_b k_b}$ obtained from the *in-situ* calibration, where ρ_b, c_b, and k_b are the density, specific heat capacity, and thermal conductivity of the basecoat layer, respectively. The side wall–upstream data were evaluated over a shorter 0.3 ms window, between the incident and reflected shocks, to assess performance under more transient conditions (shorter duration and lower frame rate). The experimental configurations for each location are summarized in Table 3.

Table 3: High-speed camera and postprocessing setups for each case.

Parameter	End wall	Side wall–downstream	Side wall–upstream
Location (x) [mm]	200	195	90
Camera resolution [pixel × pixel]	48 × 128 (z × y)	512 × 160 (x × y)	
Frame rate [fps]	840,000	200,000	
Exposure time [μs]	0.71	4.5	
Pixel size [mm]	0.50	0.39	
Measurement duration [ms]	0.9		0.3
TC comparison	TC2		TC1
Spatial average	30 × 16	9 × 23	

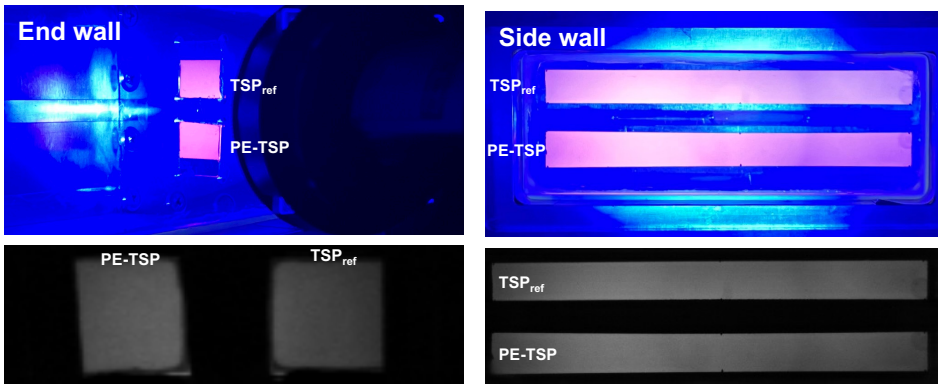
As shown in Fig. 4 and Fig. 5b, the mounting plates for both walls were designed to accommodate two different TSP formulations simultaneously, enabling direct comparison under identical flow and illumination conditions. On the side wall, a 200 mm-long plate was used, while square plates (20 × 20 mm) were installed at the end wall. The outer 2.5 mm edge of each plate was left unpainted to facilitate handling during installation.



(a) (b)

Fig. 5: (a) Schematic of sensor and image data acquisition setup and (b) isometric view of the test section.

The TSP intensity data was recorded using a 12-bit high-speed camera (V2011, Phantom). The LED light source, lens, and optical filters were configured identically to those used in the calibration chamber, as illustrated in Fig. 5a and shown in Fig. 6. The camera settings for each section are also summarized in Table 3. For the end wall, signals were spatially averaged over 30×16 pixels (corresponding to 15×8 mm). For the side wall, 9×23 pixels (corresponding to 3×9 mm) were averaged for both upstream and downstream locations. Because the primary objective was to assess SNR, temporal filter was intentionally minimized: only a 3-point moving-average filter was applied to the intensity data.



(a) (b)

Fig. 6: Color (top) and optically filtered monochrome images (bottom) for (a) the end wall and (b) the side wall.

As illustrated in Fig. 5, two fast-response E-type coaxial thermocouples (TCs) manufactured by JAXA were installed (Tanno et al. 2014), one on the end wall and one on the side wall, to enable direct heat flux comparison and *in-situ* calibration of the TSPs. In addition, two piezoelectric pressure transducers (603B1, Kistler) were mounted to measure the shock speed and reservoir pressure. All sensors and test plates were flush-mounted to minimize flow disturbance. The pressure sensors were connected to charge amplifiers (Type 5007, Kistler) with a gain of 20, while the TCs were connected to an in-house amplifier (INA128, Texas Instruments) with a gain of 500. Data acquisition was performed using a digital oscilloscope (GR-7000, Keyence) at 1 MS/s. The TC signals were filtered using a 150-point moving average, while the pressure data was low-pass filtered at 100 kHz.

For each frame i, the intensity signal $I(t)$ was converted to temperature $T(t)$ using the polynomial calibration curve obtained from the characterization experiments. The surface heat flux q_s can be computed using the classical semi-infinite heat transfer

model from Cook and Felderman (1966), which assumes that the TSP layer is sufficiently thin to be neglected and that the thermophysical properties of the basecoat layer ($\rho_b c_b k_b$) remain constant during the short test duration:

$$q_s(t_n) = 2\sqrt{\frac{\rho_b c_b k_b}{\pi}} \sum_{i=1}^{n} \frac{T(t_i) - T(t_{i-1})}{\sqrt{t_n - t_i} - \sqrt{t_n - t_{i-1}}} \tag{4}$$

where n is the total number of frames acquired. This formulation has been widely used for heat flux estimation from TSP measurements (Nagai et al. 2008; Martinez Schramm et al. 2015, 2017; Laurence et al. 2019; Risius et al. 2017). Alternative approaches have been developed to address finite TSP-layer thickness and temperature-dependent thermophysical properties, such as the semi-analytical correction of Liu et al. (2010) and the numerical inverse framework of Cai et al. (2011). While these methods offer improved accuracy in principle, their implementation requires precise thermophysical property data for both the TSP and the basecoat layers, which are not yet available for the present in-house formulations.

In this study, the method of Cook and Felderman was adopted for three main reasons. First, the TSP layer thickness was kept relatively small (2.2 μm on average), limiting finite-thickness errors. Second, both the basecoat (nitrocellulose–resin based) and TSP (PAA based) are polymeric materials, so their thermophysical properties can be assumed to be of comparable order, reducing thermophysical property-mismatch effects. Third, the wall temperature rise in both walls during the test time remained modest ($\Delta T \lesssim 10°\mathrm{C}$), such that variations in specific heat and thermal conductivity with temperature can reasonably be neglected. Under these conditions, the Cook and Felderman approach provides a sufficiently accurate and robust framework for surface heat flux recovery. The effective value of $\sqrt{\rho_b c_b k_b}$ was obtained by *in-situ* calibration against TC measurements, assuming that the heat flux at the TC and TSP surfaces is identical.

The shock tube test conditions are summarized in Table 4. Using the measured signals from the pressure sensors, the post–incident shock (subscript 2) and reservoir (subscript 5s) flow properties were calculated with the one-dimensional state-to-state solver ESTCN (Jacobs et al. 2014). The pressure ratio between the driver (p_4) and driven (p_1) sections was set to 141.8 for both the end wall and side wall experiments, which ensures a sufficient wall temperature rise within the millisecond-scale test time under both post-shock and reservoir states. A total of two experiments were conducted, one for each wall configuration. The reservoir pressure histories, shown in Fig. 7, exhibit good agreement between the two cases, indicating that the tests were carried out under nearly identical flow conditions.

Table 4: Shock tube experimental condition.

Measured parameter	Value
p_4 [kPa]	851.1
p_1 [kPa]	6.0
p_4/p_1	141.8
Shock speed [m/s]	642.2
Mach (M)	1.9
p_{5s} [kPa]	70.8
Calculated parameter	**Value**
T_2 [K]	470.19
p_2 [kPa]	22.95
U_2 [m/s]	263.08
ρ_2 [kg/m^3]	0.17
μ_2 [Pa·s]	2.56×10^{-5}
T_{5s} [K]	664.67
h_{5s} [MJ/kg]	0.67

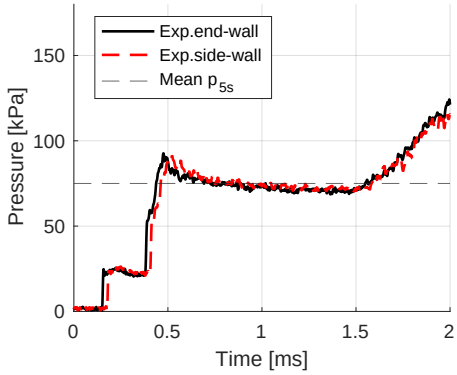


Fig. 7: Reservoir pressure histories measured at P2 (location indicated in Fig. 5a) for both end-wall and side-wall cases, showing good agreement.

3 PE-TSP Optimization and Characterization Results & Discussion

3.1 Optimization Results

The optimization results are shown in Fig. 8, where the nine cases exhibit distinct trends in both emission intensity and temperature sensitivity. Increasing C_{dye} from 50 mg/g ($\mathrm{TSP}_{\mathrm{ref}}$) to 100 mg/g ($C_{\mathrm{particle}} = 0$ wt.%) produced only a minor intensity gain of about 2% at 20 °C (Fig. 8b). In contrast, a moderate enhancement in temperature sensitivity was observed across the entire temperature range (Fig. 8c). At 20 °C, the sensitivity increased from 2.82 to 3.03 %/°C, about a 7% improvement, consistent trends with the results of Ikami et al. (2022), who also reported no further improvement beyond $C_{\mathrm{dye}} > 100$ mg/g due to concentration quenching (Grenoble et al. 2005).

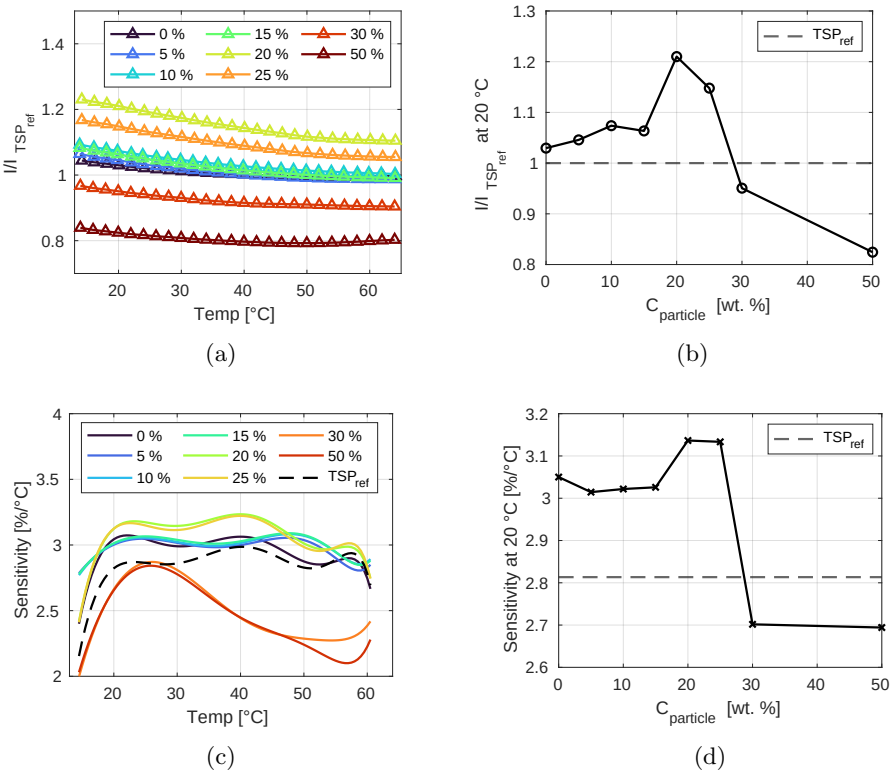


Fig. 8: Optimization results for all cases, showing (a) intensity ratio relative to the reference case ($\mathrm{TSP_{ref}}$), (b) intensity ratio at 20 °C, (c) temperature sensitivity, and (d) temperature sensitivity at 20 °C. Note that the 0 wt.% case is not identical to $\mathrm{TSP_{ref}}$; all cases shown here use the optimized dye concentration (100 mg/g), whereas $\mathrm{TSP_{ref}}$ uses 50 mg/g.

Upon adding particles, luminescence intensity increased across all temperature ranges up to $C_{\mathrm{particle}} = 20$ wt.%, after which a decline was observed. For $C_{\mathrm{particle}} \geq 30$ wt.%, intensity fell below that of $\mathrm{TSP_{ref}}$ (Fig. 8b). Temperature sensitivity remained nearly constant up to $C_{\mathrm{particle}} = 15$ wt.% (Fig. 8c), then increased between 20 and 25 wt.%. A significant drop occurred at $C_{\mathrm{particle}} = 30$ wt.%, particularly at higher temperatures. At 20 °C (Fig. 8d), the sensitivity trend followed that of the intensity, with $C_{\mathrm{particle}} = 20$ wt.% yielding the highest improvement. Based on these results, $C_{\mathrm{particle}} = 20$ wt.% was selected for the PE-TSP formulation, as it provided the

optimal balance of both luminescence intensity and temperature sensitivity. Detailed characterization of the selected PE-TSP is presented in the following section.

3.2 Characterization Results

A detailed characterization and comparison between TSP_{ref} and PE-TSP is presented in Fig. 9 and summarized in Table 5. At 20 °C, PE-TSP exhibited a 21% improvement in emission intensity relative to TSP_{ref}. The temperature sensitivity increased by 11% at 20 °C and reached a maximum across the tested temperature range of 3.3 %/°C. Pressure dependency also showed noticeable improvement: the intensity of PE-TSP remained constant up to 200 kPa and, beyond this point, decreased more slowly than that of TSP_{ref}. At 500 kPa, PE-TSP maintained nearly twice the intensity of TSP_{ref}. By contrast, photodegradation performance worsened. Initially, the intensity of PE-TSP was higher, but after approximately 130 minutes of continuous illumination it converged with that of TSP_{ref}. Linear regression of the decay slope showed a decrease rate of -4.9 %/hr for TSP_{ref} compared with -11.5 %/hr for PE-TSP, corresponding to a 135% faster degradation rate.

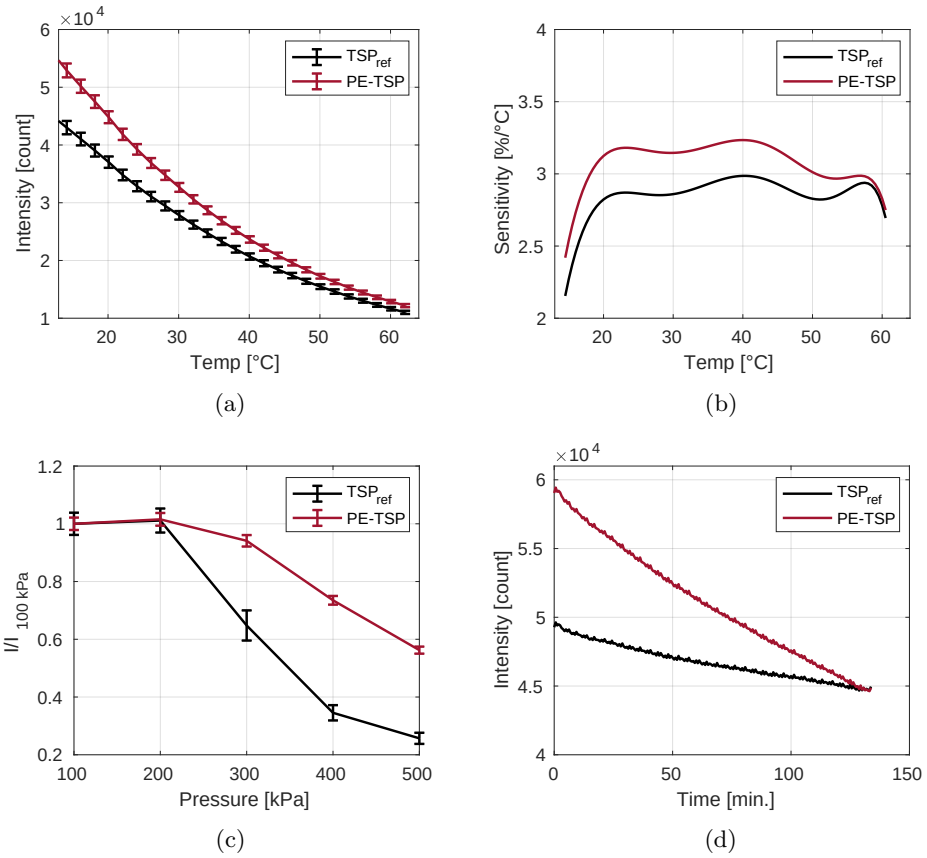
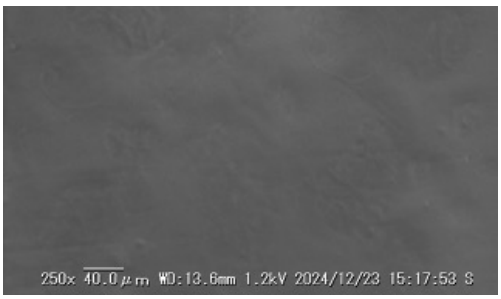


Fig. 9: Characterization of PE-TSP compared to TSP_{ref}: (a) intensity, (b) temperature sensitivity (seventh-order polynomial fit), (c) pressure dependency, and (d) photodegradation.

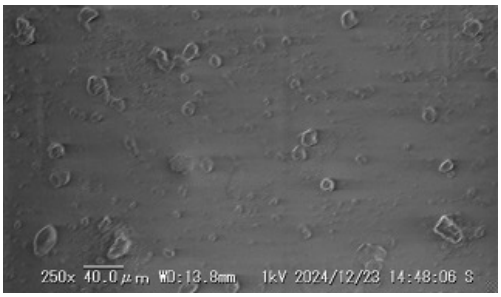
Table 5: Comparison of performance parameters between TSP_{ref} and PE-TSP. All values were measured at 20 °C.

Parameter	TSP_{ref}	PE-TSP	Δ	Percentage [%]
Intensity [count×10^4]	3.703	4.483	0.780	21
Sensitivity [%/°C]	2.82	3.12	0.30	11
Pressure ratio (I_{500kpa}/I_{100kpa})	0.275	0.551	0.276	100
Photodegradation rate [%/hr]	-4.9	−11.5	−6.6	−135

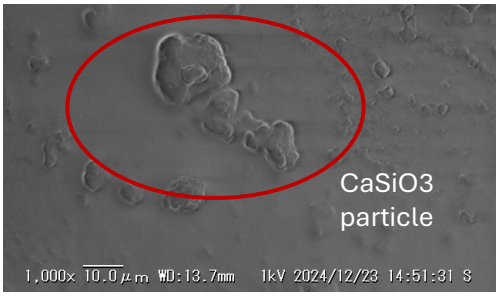
To further investigate the mechanisms underlying the enhanced performance, surface morphologies were examined using SEM (Fig. 10). The TSP_{ref} exhibited a smooth and uniform surface, whereas PE-TSP showed microscale $CaSiO_3$ particles dispersed throughout the coating layer. At higher magnification, the $CaSiO_3$ particles displayed an agglomerated microstructure. Although distinct pore structures were not resolved in the present SEM images, $CaSiO_3$ particles are widely reported to exhibit intrinsic porosity (Sunitha et al. 2013). Based on these observations and prior findings, the macroscopic mechanism illustrated in Fig. 11 is proposed.



(a)



(b)



(c)

Fig. 10: SEM images of (a) TSP_{ref}, (b) PE-TSP, and (c) $CaSiO_3$ particles on the PE-TSP surface.

The enhanced luminescence intensity and temperature sensitivity observed in the PE-TSP formulation may be attributed to optical and surface effects introduced by the incorporation of $CaSiO_3$ microparticles. The relatively high refractive index of $CaSiO_3$ can promote internal light scattering within the paint layer, thereby increasing the effective photon path length and the probability of dye excitation, as reported in

previous studies (Woo et al. 2023). In addition, because the particle diameter (7–10 ms) exceeds the mean thickness of the TSP layer, partial particle protrusion from the binder matrix can induce microscale surface roughness, which may increase the effective optical interaction area between the excitation light and the dye molecules.

The reduced pressure sensitivity of PE-TSP may be interpreted as a consequence of suppressed oxygen-quenching, resulting from the combined effects of the PAA binder and the porous structure of $CaSiO_3$ particles acting as a host matrix for Ru(phen), as suggested in the literature (Sunitha et al. 2013; Liu et al. 2017; Othman et al. 2021). In the present study, this interpretation is inferred from previously reported microstructural and oxygen permeability characteristics of similar particle-based TSP systems; direct supporting measurements, such as cross-sectional SEM imaging resolving pore networks or oxygen permeability characterization, were beyond the scope of the present study.

The accelerated photodegradation may, on the other hand, be attributed to photocatalytic activity at the $CaSiO_3$ surface under continuous illumination, whereby photo-generated electrons (e^-) and holes (h^+) induce oxidation reactions that enhance oxygen-quenching and progressively reduce emission intensity (Karami et al. 2022). Nevertheless, this effect is negligible in high-speed impulse facilities, where illumination is triggered for only a few milliseconds and total test durations typically remain below 10 ms.

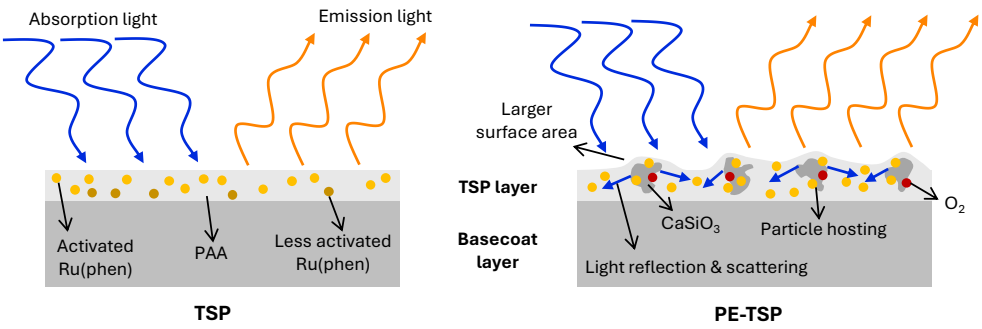


Fig. 11: Schematic of the PE-TSP mechanism for enhanced luminescence, sensitivity, and reduced pressure dependence.

4 PE-TSP Validation Results & Discussion

The heat flux data from TCs are shown in Fig. 12, and the transformation from intensity to temperature and subsequently to heat flux for all three cases is presented in Fig. 13. The normalized intensity plot highlights the larger change in signal level of PE-TSP relative to $\mathrm{TSP_{ref}}$, consistent with its enhanced temperature sensitivity. After conversion to temperature using the polynomial calibration curve, both TSPs exhibit identical temporal behavior. This indicates that, although $CaSiO_3$ particles were incorporated into the TSP formulation and may have altered the effective thermophysical properties of the TSP layer, the transient temperature response remains unaffected under the same heat load. Also, local particle agglomeration within the PE-TSP layer, if present, could introduce spatial inhomogeneity in the effective thermal resistance and locally attenuate the thermal response; however, such effects were not observed in the present measurements, consistent with the use of continuous ultrasonic agitation and uniform spray application during coating. Accordingly, the surface heat flux is primarily governed by the thermophysical properties of the basecoat layer.

A sharp increase in temperature near $t = 0.2$ ms at the end wall and and side wall–downstream, and at $t = 0.1$ ms at the side wall–upstream corresponds to the

arrival of the incident shock. The regions highlighted in yellow denote the test time used for calculating the mean and STD for comparison. It should be noted that the end wall and side wall–downstream locations capture the flow in the post–triple-point reservoir region (region 5s), whereas the side wall–upstream location captures the flow immediately behind the incident shock (region 2). Further discussion of these flow-region is provided later in this section.

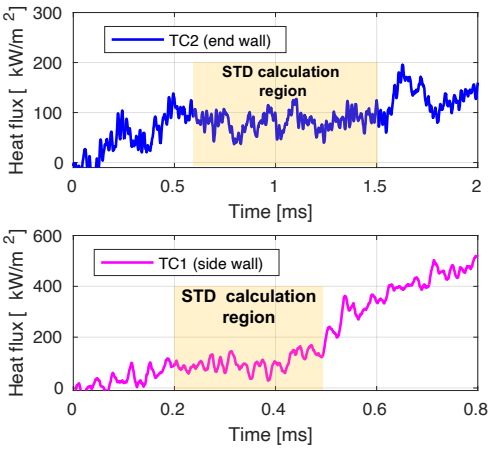


Fig. 12: Transient wall heat flux measured by TCs.

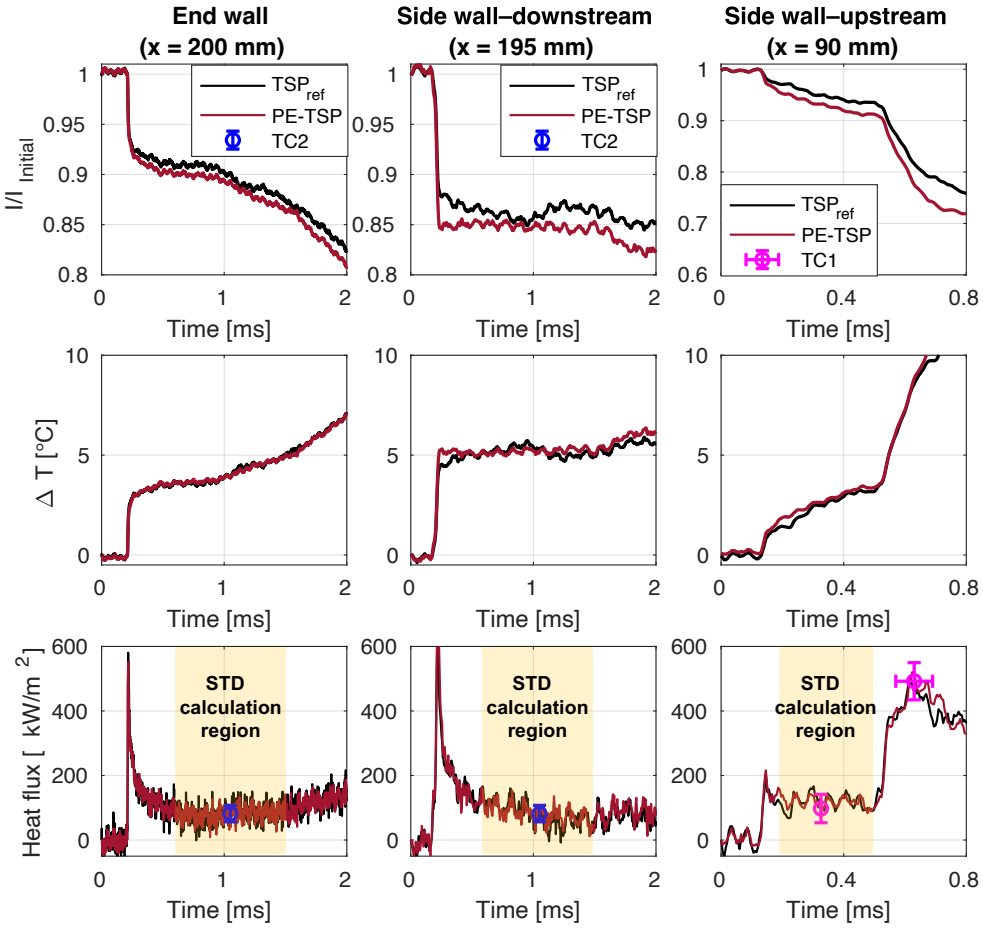


Fig. 13: TSP measurements showing the transformation from intensity (top) to temperature (middle) and to heat flux (bottom) for three cases: end wall (right), side wall–downstream (center), and side wall–upstream (left). Yellow regions indicate the test time used for calculating the mean and STD.

From the *in-situ* calibration at the end wall, the thermophysical parameter $\sqrt{\rho_b c_b k_b}$ of the basecoat was determined to be 760 ± 3 $\mathrm{Jm^{-2}K^{-1}s^{-1/2}}$. To evaluate the influence of finite TSP layer thickness, the expression from Schultz and Jones (1973) was employed following the approach of Ozawa et al. (2015):

$$q_m/q_{s0} = 1 - \frac{L_p}{\sqrt{\pi \alpha_p t}} \left(\frac{1}{a} - \frac{a}{2} \right), \tag{5}$$

where subscript p refers to TSP layer properties, and $a = \sqrt{\rho_b c_b k_b / \rho_p c_p k_p}$. Using $\sqrt{\rho_p c_p k_p} = 882$ Jm^{-2}K^{-1}s$^{-1/2}$ reported by Ozawa et al. (2015), which employed the same PAA binder in their TSP formulation, the predicted error plot shown in Fig. 14 indicates that the heat flux may deviate by approximately 4% over the end wall test time ($t \sim O(1)$ ms), due to the slightly higher $\sqrt{\rho_p c_p k_p}$ of the TSP layer compared with the basecoat layer. Even under shorter test time of $t \sim O(0.1)$ ms, such as during side wall incident shock arrival, the error remains limited to within 10% and decreases with increasing timescale. Considering that the overall experimental uncertainty of TSP-based heat flux measurements ranges from 13% to 43% (Table 6), the finite-thickness error is expected to have a minor influence on the results.

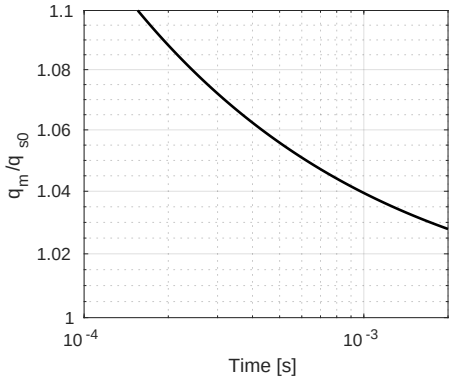


Fig. 14: Estimated time-dependent error range associated with neglecting finite TSP layer thickness.

The $\sqrt{\rho_b c_b k_b}$ value obtained from the end wall *in-situ* calibration was also applied to the side wall cases. Table 6 summarizes the mean heat flux and STD for both TSPs and TCs during the test period. The uncertainty of the TC measurements mainly arises from the small temperature rise in TC under the present conditions, resulting in millivolt-level output signals that are more susceptible to electronic noise, including amplifier noise and ambient AC interference. This effect is particularly pronounced in the side wall–upstream case due to its short test duration.

The mean values from the TSPs agree well with those from TCs, within the uncertainty range. The heat flux plots for all cases (Fig. 13) show that the oscillation amplitude of PE-TSP is consistently lower than that of TSP_{ref}. For the downstream cases (the end wall and side wall–downstream), PE-TSP exhibits STD reductions of 21.39% and 22.17%, respectively, relative to TSP_{ref} (Table 6). Although the magnitude of reduction percentage is similar, the side wall–downstream case shows higher absolute STDs for both TSPs. This result indicates that the higher camera frame rate effectively reduces the absolute STD, but the relative STD reduction between the two TSPs remains essentially independent of frame rate. For the side wall–upstream case, PE-TSP shows a 33.18% STD reduction, suggesting that the benefit is more pronounced when the measurement duration is shorter.

Table 6: Mean and STD of heat flux measurements for TSPs and corresponding TCs for three cases.

Method		TC		TSP_{ref}		PE-TSP		PE-TSP
Parameter	Location (x) [mm]	Mean [kW/m^2]	STD	Mean [kW/m^2]	STD	Mean [kW/m^2]	STD	STD reduction [%]
End wall	200	81.95	25.51	80.95	25.30	80.19	19.89	21.39
Side wall –downstream	195			80.09	35.07	81.12	27.30	22.17
Side wall –upstream	90	97.51	44.03	116.25	24.09	116.71	16.10	33.18

The reduced STD of PE-TSP indicates that it provides a higher SNR compared with TSP_{ref}. In TSP measurements, the dominant noise sources typically originate from (1) intensity oscillations of the LED light source, (2) camera readout and dark-current noise, (3) pressure dependency, and (4) self-illumination of the test gas in high-enthalpy conditions. Because PE-TSP exhibits both higher luminescent intensity and greater temperature sensitivity, the signal level is intrinsically stronger. Furthermore, the reduced pressure dependency of PE-TSP lowers the noise. Together, these factors

enhance the effective SNR, which can be expressed conceptually as

$$SNR = \frac{\text{TSP signal}}{\begin{array}{c}\text{LED oscillation + camera noise} \\ \text{+ pressure dependency + self-illumination}\end{array}}. \tag{6}$$

This improvement in SNR explains the lower oscillation amplitudes and lower STD observed in the PE-TSP heat flux traces compared to TSP_{ref}.

Given this intrinsic SNR advantage, the next step was to examine whether additional postprocessing could further enhance signal quality. A sensitivity analysis on the moving-average window size was therefore performed (Fig. 15). The three cases exhibited distinct behaviors: nearly constant for the end wall, an increasing trend for the side wall–downstream, and a decreasing trend for the side wall–upstream. These results demonstrate that enlarging the moving-average window does not necessarily improve accuracy or reduce uncertainty in TSP-based heat flux measurements. In addition, particularly in the side wall–upstream case, excessively large windows oversmooth the sharp heat flux rises associated with the passage of incident and reflected shocks, leading to inaccurate measurement during the quasi-steady test time.

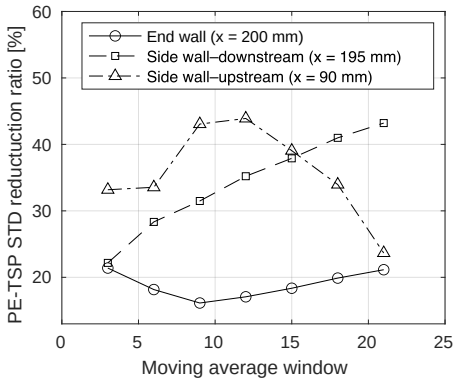


Fig. 15: Sensitivity analysis of the moving-average window size on the STD reduction ratio for the three measurement cases.

Using PE-TSP on the side wall, unsteady two-dimensional flow phenomena inside the shock tube were analyzed. A 3×3 spatial average was applied to the 2D data, followed by an additional 5-point moving-average filter to the heat flux signal. As shown in Fig. 16, the incident shock propagates through the test section, causing an initial rise in surface heat flux. During this propagation, debris from the ruptured diaphragm occasionally passed through the optical field, locally darkening the TSP signal. Because TSP intensity is inversely proportional to temperature, these darkened regions appear as artificially heated spots.

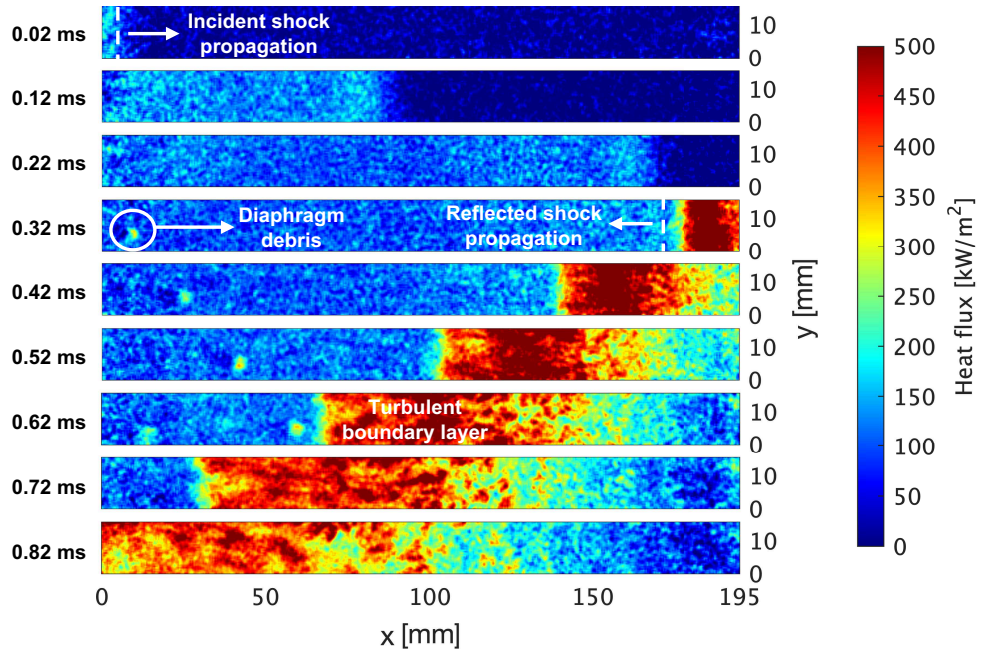


Fig. 16: Temporal evolution of the two-dimensional wall heat flux field measured by PE-TSP as the incident and reflected shocks propagate along the side wall. Snapshots are shown at 0.1 ms intervals. The corresponding movie is provided as online supplementary material.

Notably, no boundary layer transition front was observed following the passage of the incident shock, as indicated by the absence of localized heat flux peaks or distinct spatio-temporal transition signatures (Fig. 16). In time-resolved TSP measurements

of shock tube boundary layers, laminar–turbulent transition is typically characterized by an abrupt increase in surface heat flux accompanied by an upstream-propagating transition front or turbulent streak-like structures; no such features were detected under the present conditions. This behavior is consistent with the minimized wall discontinuities in the present setup: the square-section shock tube eliminates geometric transitions around the TSP plates, and all sensors and test plates were flush-mounted to maintain a smooth wall surface.

To further assess the potential influence of surface roughness on boundary layer transition, a quantitative estimate of the laminar boundary layer thickness was performed for the incident shock condition at $M = 1.9$. Using the post–incident shock flow velocity U_2 and the region 2 test duration $\Delta t = 0.3$ ms, the effective development length was estimated as $x_{eff} = U_2 \Delta t \approx 78.90$ mm, which is smaller than the test section length ($L = 200$ mm). The boundary layer thickness was then estimated using the standard laminar flat plate scaling

$$\delta_{99} \approx \frac{5x_{eff}}{\sqrt{Re_{x_{eff}}}}, \qquad Re_{x_{eff}} = \frac{\rho_2 U_2 x_{eff}}{\mu_2}, \tag{7}$$

where ρ_2 and μ_2 are the density and dynamic viscosity in region 2, respectively, as summarized in Table 4. Substituting the corresponding values yields $\delta_{99} \approx 1.06$ mm over the measurement region.

The effective surface roughness was conservatively taken to be on the order of the $CaSiO_3$ particle diameter ($k \sim 10$ μm), which provides an upper bound for coating-induced roughness since the mean TSP layer thickness is smaller than the particle size. Even under this conservative assumption, the ratio $k/\delta_{99} \sim 9.1 \times 10^{-3} \ll 1$, consistent with the absence of boundary layer transition signatures in the present measurements. Although the quantitative estimate is presented for $M = 1.9$, the same scaling is

expected to apply at higher Mach numbers under comparable short-duration impulse ground-testing facility conditions.

The shock is then reflected at the end wall, producing a much stronger compression than that associated with the incident shock. This reflection generates an abrupt rise in temperature, resulting in a pronounced peak in wall heat flux immediately after the reflected shock passes, as observed for both the end wall and side wall–downstream cases (Fig. 13). Following reflection, the flow remains strongly unsteady; the reflected shock interacts with the developing boundary layer, steepening near-wall temperature gradients and sustaining elevated heat flux levels during the short transient period (Mark 1958).

Following the large peak, a nearly constant heat flux region appears, corresponding to the reservoir condition (region 5s), as shown in the x–t diagram (Fig. 17). The x–t diagram was extracted along the horizontal centerline of the 2D data, and the movie of both Fig. 16 and Fig. 17 is provided as online supplementary material. The average heat flux measured in this region was slightly lower than that obtained after the incident shock at the upstream side wall, consistent with the mean heat flux values summarized in Table 6 and Fig. 13. This difference arises from the distinct flow structures and heat transfer mechanisms in the two regions. Immediately behind the incident shock (region 2), the compressed gas flowing past the side wall forms a thin laminar boundary layer with steep velocity and temperature gradients, producing strong convective heat transfer (Mirels 1956). In contrast, after reflection at the end wall, the test gas becomes nearly stagnant. Although this region exhibits higher static temperature and pressure, near-wall shear and convective transport are diminished, and heat transfer becomes predominantly diffusion-driven (Cook 1972). The slower, conduction-dominated temperature evolution at the end wall therefore yields a smaller heat-flux magnitude compared with the convective heat flux observed along the side wall.

Near $x = 0$–50 mm and around $t = 1.5$ ms, the reflected shock interacts with the contact surface and re-enters the test section. The diagonal streaks appearing at later times correspond to these contact-surface interactions and to turbulent streak structures, marking the end of the effective test duration. Additionally, faint horizontal bands, more pronounced on the downstream side, indicate LED flicker noise originating from the right-side illumination, confirming the primary optical noise source in this setup.

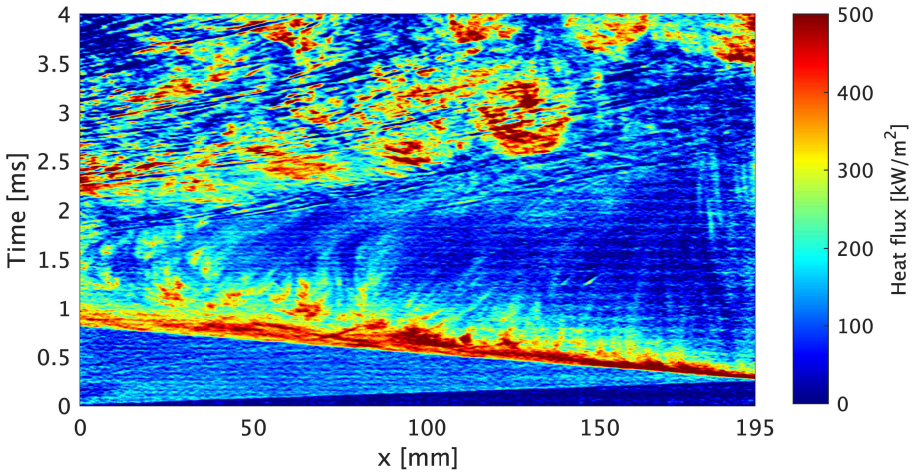


Fig. 17: Heat flux x–t diagram using PE-TSP on the side wall. The corresponding movie is provided as online supplementary material.

5 Conclusion

A particle-enhanced temperature-sensitive paint (PE-TSP) based on Ru(phen)/PAA with $CaSiO_3$ microparticles was developed and validated for high-speed aerothermodynamic applications. Calibration tests showed that particle addition increased luminescence by 21% and temperature sensitivity by 11% relative to the reference formulation, along with reduced pressure dependency (approximately twice the emission at 500 kPa). Although PE-TSP exhibited increased photodegradation, this effect can

be mitigated by pulsed LED illumination lasting only a few milliseconds, typical of impulse ground-testing facilities.

Through detailed characterization, the performance gain was found to arise from enhanced light scattering, increased surface area, and dual protection against oxygen-quenching provided by the PAA binder and porous $CaSiO_3$ structure. Shock tube experiments confirmed improved signal quality under high-speed and high-temperature conditions: PE-TSP produced heat flux histories consistent with thermocouple data and reduced oscillation amplitude, achieving up to 33% lower standard deviation than the reference formulation. Moreover, two-dimensional heat flux visualization demonstrated the capability of PE-TSP to resolve unsteady flow phenomena in shock-driven environments. Future work will focus on advancing TSP measurement capability through the integration of high quantum-efficiency LED technologies, detailed thermophysical characterization, and application of PE-TSP to high-enthalpy hypersonic flow environments.

Acknowledgements. The authors would like to thank Dr. Hideyuki Tanno for technical support with the thermocouples, and Mr. Koichi Takahashi and Mr. Toshihiro Ogawa for their technical support with the experimental setup.

Competing interests. The authors declare that they have no known competing financial interests or personal relationships that could have appeared to influence the work reported in this paper.

Data availability. The data that support the findings of this study are available from the corresponding author upon reasonable request.

CRediT authorship contribution statement. **Jinyoung Kim**: Methodology, Software, Validation, Formal analysis, Investigation, Data curation, Writing – original draft, Visualization. **Mithat Engin**: Methodology, Formal analysis, Investigation,

Data curation, Visualization. **Masaki Okawa**: Methodology, Validation, Investigation. **Tsubasa Ikami**: Methodology, Software, Validation, Investigation, Writing – review & editing. **Bok Jik Lee**: Methodology, Resources, Writing – review & editing, Funding acquisition. **Hiroki Nagai**: Conceptualization, Methodology, Resources, Data curation, Writing – review & editing, Supervision, Project administration, Funding acquisition.

References

Cook, W.J., Felderman, E.J.: Reduction of data from thin-film heat-transfer gages - A concise numerical technique. AIAA Journal **4**(3), 561–562 (1966) https://doi.org/10.2514/3.3486

Cai, Z., Liu, T., Wang, B., Rubal, J., Sullivan, J.P.: Numerical Inverse Heat Transfer Analysis for Temperature-Sensitive-Paint Measurements in Hypersonic Tunnels. Journal of Thermophysics and Heat Transfer **25**(1), 59–67 (2011) https://doi.org/10.2514/1.49217

Cook, W.J.: Prediction and measurement of heat transfer rates for the shock-induced unsteady laminar boundary layer on a flat plate (1972)

Egami, Y., Fey, U., Klein, C., Quest, J., Ondrus, V., Beifuss, U.: Development of new two-component temperature-sensitive paint (TSP) for cryogenic testing. Measurement Science and Technology **23**(11), 115301 (2012) https://doi.org/10.1088/0957-0233/23/11/115301

Fey, U., Engler, R.H., Egami, Y., Iijima, Y., Asai, K., Jansen, U., Quest, J.: Transition detection by temperature sensitive paint at cryogenic temperatures in the European Transonic Wind tunnel (ETW). In: 20th International Congress on Instrumentation

in Aerospace Simulation Facilities, 2003. ICIASF '03., pp. 77–88 (2003). https://doi.org/10.1109/ICIASF.2003.1274855

Grenoble, S., Gouterman, M., Khalil, G., Callis, J., Dalton, L.: Pressure-sensitive paint (psp): concentration quenching of platinum and magnesium porphyrin dyes in polymeric films. Journal of Luminescence **113**(1), 33–44 (2005) https://doi.org/10.1016/j.jlumin.2004.08.049

Hubner, J.P., Carroll, B.F., Schanze, K.S., Ji, H.F., Holden, M.S.: Temperature- and Pressure-Sensitive Paint Measurements in Short-Duration Hypersonic Flow. AIAA Journal **39**(4), 654–659 (2001) https://doi.org/10.2514/2.1358

Hubner, J.P., Carroll, B.F., Schanze, K.S.: Heat-Transfer Measurements in Hypersonic Flow Using Luminescent Coating Techniques. Journal of Thermophysics and Heat Transfer **16**(4), 516–522 (2002) https://doi.org/10.2514/2.6726

Horagiri, T., Nagai, H.: Development of Temperature-Sensitive Paint with High Performance and Responsibility for Aerodynamic Heating Measurement. In: 52nd Aerospace Sciences Meeting. American Institute of Aeronautics and Astronautics, National Harbor, Maryland (2014). https://doi.org/10.2514/6.2014-1408

Ikami, T., Fujita, K., Nagai, H.: Influence of Formulations on Characteristics of Ruthenium-Based Temperature-Sensitive Paints. Sensors **22**(3), 901 (2022) https://doi.org/10.3390/s22030901

Ikami, T., Nishimura, R., Nagai, H.: cntTSP visualization technique for rotating blade surface flow at low Reynolds number. Experiments in Fluids **65**(2), 14 (2015) https://doi.org/10.1007/s00348-023-03757-x

Jacobs, P.A., Gollan, R.J., Potter, D.F., Zander, F., Gildfind, D.E., Blyton, P., Chan, W.Y.K., Doherty, L.: Estimation of high-enthalpy flow conditions for simple shock

and expansion processes using the ESTCj program and library. Technical report, University of Queensland, St. Lucia, Queensland, Australia (2014)

Kim, J., Kim, J., Hur, J., Lee, B.J., Jeung, I.-S.: Nozzle Flow Characterization of the SNU Hypersonic Shock Tunnel. International Journal of Aeronautical and Space Sciences **26**(3), 953–962 (2025) https://doi.org/10.1007/s42405-024-00806-5

Karami, M., Yousif, Q.A., Ghanbari, M., Mahdavi, K., Salavati-Niasari, M.: Green fabrication of graphene quantum dots from cotton with casio3 nanostructure and enhanced photocatalytic performance for water treatment. International Journal of Hydrogen Energy **47**(11), 7228–7241 (2022) https://doi.org/10.1016/j.ijhydene.2021.12.071

Liu, T., Cai, Z., Lai, J., Rubal, J., Sullivan, J.P.: Analytical Method for Determining Heat Flux from Temperature-Sensitive-Paint Measurements in Hypersonic Tunnels. Journal of Thermophysics and Heat Transfer **24**(1), 85–94 (2010) https://doi.org/10.2514/1.43372

Lang, W., Gardner, A.D., Mariappan, S., Klein, C., Raffel, M.: Boundary-layer transition on a rotor blade measured by temperature-sensitive paint, thermal imaging and image derotation. Experiments in Fluids **56**(6), 118 (2015) https://doi.org/10.1007/s00348-015-1988-5

Laurence, S.J., Ozawa, H., Martinez Schramm, J., Butler, C.S., Hannemann, K.: Heat-flux measurements on a hypersonic inlet ramp using fast-response temperature-sensitive paint. Experiments in Fluids **60**(4), 70 (2019) https://doi.org/10.1007/s00348-019-2711-8

Liu, T., Sullivan, J.P., Asai, K., Klein, C., Egami, Y.: Pressure and Temperature Sensitive Paints. Experimental Fluid Mechanics. Springer, Cham (2021). https://

doi.org/10.1007/978-3-030-68056-5

Liu, J., Wang, N., Yu, Y., Yan, Y., Zhang, H., Li, J., Yu, J.: Carbon dots in zeolites: A new class of thermally activated delayed fluorescence materials with ultralong lifetimes. Science Advances **3**(5), 1603171 (2017) https://doi.org/10.1126/sciadv.1603171

Mark, H.: The Interaction of a Reflected Shock Wave with the Boundary Layer in a Shock Tube (1958)

Mirels, H.: Boundary layer behind shock or thin expansion wave moving into stationary fluid (1956)

Martinez Schramm, J., Edzards, F., Hannemann, K.: Development of Ultra-fast Temperature Sensitive Paints for Hypersonic High Speed Flows. In: 21st AIAA International Space Planes and Hypersonics Technologies Conference. American Institute of Aeronautics and Astronautics, Xiamen, China (2017). https://doi.org/10.2514/6.2017-2211

Martinez Schramm, J., Hannemann, K., Ozawa, H., Beck, W., Klein, C.: Development of Temperature Sensitive Paints in the High Enthalpy Shock Tunnel Göttingen, HEG. In: 8th European Symposium on Aerothermodynamics for Space Vehicles, Lisbon, Portugal, pp. 1–7 (2015)

Nagayama, T., Nagai, H., Tanno, H., Komuro, T.: Visualization of Hypersonic Boundary Layer Transition on Elliptic Cone in High Enthalpy Shock Tunnel with Temperature-Sensitive Paint. In: 54th AIAA Aerospace Sciences Meeting. American Institute of Aeronautics and Astronautics, San Diego, California, USA (2016). https://doi.org/10.2514/6.2016-0358

Nagayama, T., Nagai, H., Tanno, H., Komuro, T.: Global Heat Flux Measurement

Using Temperature-Sensitive Paint in High-Enthalpy Shock Tunnel HIEST. In: 55th AIAA Aerospace Sciences Meeting. American Institute of Aeronautics and Astronautics, Grapevine, Texas (2017). https://doi.org/10.2514/6.2017-1682

Nakakita, K., Osafune, T., Asai, K.: Global Heat Transfer Measurement in a Hypersonic Shock Tunnel Using Temperature-Sensitive Paint. In: 41st Aerospace Sciences Meeting and Exhibit. American Institute of Aeronautics and Astronautics, Reno, Nevada (2003). https://doi.org/10.2514/6.2003-743

Nagai, H., Ohmi, S., Asai, K., Nakakita, K.: Effect of Temperature-Sensitive-Paint Thickness on Global Heat Transfer Measurement in Hypersonic Flow. Journal of Thermophysics and Heat Transfer **22**(3), 373–381 (2008) https://doi.org/10.2514/1.34152

Nagai, H., Swamura, R., Asai, K.: Experimental Study of Heat Transfer Measurement using Temperature-Sensitive Paint for High-Temperature Application in Hypersonic Flow. In: 49th AIAA Aerospace Sciences Meeting Including the New Horizons Forum and Aerospace Exposition. American Institute of Aeronautics and Astronautics, Orlando, Florida (2011). https://doi.org/10.2514/6.2011-850

Othman, H.O., Hassan, R., Faizullah, A., Ghadiri, M.: A carbon-based fluorescent probe (n-cds) encapsulated in a zeolite matrix (nafz) for ultrasensitive detection of hg (ii) in fish. Talanta **234**, 122646 (2021) https://doi.org/10.1016/j.talanta.2021.122646

Ozawa, H., Laurence, S.J.: Experimental investigation of the shock-induced flow over a wall-mounted cylinder. Journal of Fluid Mechanics **849**, 1009–1042 (2018) https://doi.org/10.1017/jfm.2018.433

Ozawa, H., Laurence, S.J., Schramm, J.M., Wagner, A., Hannemann, K.: Fast-response

temperature-sensitive-paint measurements on a hypersonic transition cone. Experiments in Fluids **56**(1), 1853 (2015) https://doi.org/10.1007/s00348-014-1853-y

Ozawa, H.: Experimental study of unsteady aerothermodynamic phenomena on shock-tube wall using fast-response temperature-sensitive paints. Physics of Fluids **28**(4), 046103 (2016) https://doi.org/10.1063/1.4947040

Petersen, A., Hilfer, M.: Boundary layer analysis of a transonic high-pressure turbine vane using ultra-fast-response temperature-sensitive paint. Journal of Turbomachinery **146**(9), 091013 (2024) https://doi.org/10.1115/1.4065739

Peng, D., Jiao, L., Sun, Z., Gu, Y., Liu, Y.: Simultaneous PSP and TSP measurements of transient flow in a long-duration hypersonic tunnel. Experiments in Fluids **57**(12), 188 (2016) https://doi.org/10.1007/s00348-016-2280-z

Paull, A., Stalker, R.: Scramjet testing in the T4 impulse facility. In: 8th AIAA International Space Planes and Hypersonic Systems and Technologies Conference. American Institute of Aeronautics and Astronautics, Norfolk,VA,U.S.A. (1998). https://doi.org/10.2514/6.1998-1533

Risius, S., Beck, W.H., Klein, C., Henne, U., Wagner, A.: Determination of heat transfer into a wedge model in a hypersonic flow using temperature-sensitive paint. Experiments in Fluids **58**(9), 117 (2017) https://doi.org/10.1007/s00348-017-2393-z

Schultz, D.L., Jones, T.V.: Heat-transfer Measurements in Short-duration Hypersonic Facilities. Technical report (1973)

Sunitha, D.V., Nagabhushana, H., Sharma, S.C., Nagabhushana, B.M., Chakradhar, R.P.S.: Luminescent characteristics of Eu3+ doped di-calcium silicate nano-powders for white LEDs. Journal of Alloys and Compounds **575**, 434–443 (2013) https://doi.org/10.1016/j.jallcom.2013.05.132

Tanno, H., Komuro, T., Sato, K., Itoh, K., Yamada, T., Sato, N., Nakano, E.: Heat flux measurement of Apollo capsule model in the free-piston shock tunnel HIEST. In: 16th AIAA/DLR/DGLR International Space Planes and Hypersonic Systems and Technologies Conference. American Institute of Aeronautics and Astronautics, Bremen, Germany (2009). https://doi.org/10.2514/6.2009-7304

Tanno, H., Komuro, T., Sato, K., Itoh, K., Lillard, R.P., Olejniczak, J., Grinstead, J.H.: Aeroheating measurement of Apollo shaped capsule with boundary layer trip in the free-piston shock tunnel HIEST. In: 52nd Aerospace Sciences Meeting. American Institute of Aeronautics and Astronautics, National Harbor, Maryland (2014). https://doi.org/10.2514/6.2014-0434

Woo, H.-J., Chung, S.-J., Hill, M.L., Hadrick, K., Kim, T.: Europium-doped calcium silicate nanoparticles as high-quantum-yield red-emitting phosphors. ACS Applied Nano Materials **6**(11), 9884–9891 (2023) https://doi.org/10.1021/acsanm.3c01547

Supplementary Files

This is a list of supplementary files associated with this preprint. Click to download.

- supplementarymaterial.mp4